*Progress In Electromagnetics Research B, Vol. 85, 65–83, 2019*

# Design and Analysis of a Broadband High Isolation Dual-Polarized Omnidirectional Antenna

**Yuwei Zhang, Shu Lin*, Shang Yu, Shoulan Liu, Guanjun Liu, and Alexander Denisov**

**Abstract**—A high isolation broadband dual-polarized omnidirectional antenna comprising two low profile orthogonally polarized omnidirectional radiating elements is presented. A modified monopole using loadings to broaden impedance bandwidth is applied to vertical polarization (VP), while four printed concentrically arranged Yagi-Uda-like antennas are employed for horizontal polarization (HP). Both the simulated and measured results indicate that the operating bands of the proposed antenna with its reflection coefficient less than −10 dB are 1.48 to 3.16 GHz for VP and 1.69 to 2.7 GHz for HP. A good port isolation larger than 40 dB and omnidirectional patterns with the out-of-roundness less than 2 dB in horizontal plane are obtained. This paper explains the radiation mechanism by investigating the simulated surface current distributions for VP element and establishing a radiation model for HP element, and also analyzes the performance of the proposed antenna. This antenna design can be applied to 4G (LTE) communication system.

## 1. INTRODUCTION

With the rapid development of mobile communication technology, the communication system is required to have a broad bandwidth. Recently, the band of 4G communication system has already covered the range of 1710–2690 MHz [1], so that the antennas acting as the front-end of communication system should be operated in that frequency range. Even though the 5G communication technology is coming and has become one of the hot research issues, because of the large amount of coverage, 4G antennas will still play a key role in the communication service in the further years. Moreover, owing to the merits of 360° full coverage radiation in the horizontal plane and supporting a free alignment between receiving and transmitting antennas, omnidirectional antennas have been widely used in base stations [2–5]. On the other hand, due to the properties of enhancing the channel capacity and mitigating multipath fading, dual-polarized antennas possessing two orthogonal electrical field components in the direction of radiation are also extensively applied in many modern communication systems [6]. However, the requirement of isolation between the ports for HP and VP in the dual-polarized base station antenna is usually larger than 30 dB [7]. Thus, considering the aforementioned requirements and design constrains, the design of an antenna with dual-polarized diversity, high isolation, omnidirectional radiation, broad bandwidth covering the 4G band, and low-profile height (lower height of its profile) is facing crucial challenge.

As a typical VP antenna, a monopole antenna possesses omnidirectional radiation characteristic. Recently, a type of printed antenna [8–11] composed of two identical perpendicular positioned monopoles has been designed for dual-polarized omnidirectional radiation; however, the profile height is larger than $0.1\lambda_L$ at the lowest operating frequency. Another type of dual-polarized omnidirectional antenna is the combination of a circular HP antenna and a VP monopole antenna. Because of broadband, low-profile, and omnidirectional radiation characteristics, this type of antennas suitable for indoor base stations

*Received 13 May 2019, Accepted 18 July 2019, Scheduled 30 July 2019*
* Corresponding author: Shu Lin (linshu@hit.edu.cn).
The authors are with the School of Electronics and Information Engineering, Harbin Institute of Technology, China.

has drawn tremendous attention; meanwhile, the designers keep making improvements for this kind of antennas to achieve excellent performance. [12] is a broadband dual-polarized and omnidirectional antenna with operating band of 1.8–2.7 GHz (35%) for HP and 0.806–0.96 GHz (17.4%) for VP. The port isolation reaches 25 dB, and the height of its profile is 110 mm. Compared with the preceding antenna, [13] ameliorates the antenna performance of bandwidth and profile height. The bandwidth can cover 4G network band, and the low-profile height can be reduced to 102.6 mm. Two-port isolation of 25 dB can be obtained. [14] is a broadband dual-polarized omnidirectional antenna employing four shorting legs and a printed broadband balun. Its bandwidth ranges from 1.7 to 2.7 GHz; low-profile height is as low as 97.5 mm; and port isolation is larger than 31 dB. Consequently, the performance is improved again. In order to decrease the profile height efficiently and enhance the impedance bandwidth simultaneously, the antenna presented in [15] adopts an AMC reflector; however, due to the limitation of the distance between two elements, the isolation between the two ports is only about 20 dB. By combining two circular HP elements and one VP element which has three radiation patches with a discone shape's external profile, the dual-polarized antenna designed in [16] can realize multiband characteristic with broad operating band, whereas the profile height is large of 117.5 mm, and the isolations larger than 25 dB at 1.69–3.75 GHz and 14 dB at 690–1.03 GHz are provided. Paper [17] also proposes a dual-polarized dual-band omnidirectional antenna comprising two circular HP elements and one VP element, and the profile height of this antenna is still higher than 100 mm and the port isolation larger than 20 dB. In [18], an antenna array arranged by eight dual-polarized antenna elements has been proposed. Its array elements possess the profile height of 72 mm and good port isolation of 40 dB, but the bandwidth is as narrow as 25% (1.7–2.2 GHz). Considering the above-mentioned antennas, it can be seen clearly that it is so hard to achieve a perfect antenna design target with broad bandwidth, low profile, and good isolation simultaneously.

In this paper, a broadband dual-polarized and omnidirectional antenna with two different polarized low-profile radiation elements is studied. This antenna realizes omnidirectional radiation performance in both the VP and HP elements, and two orthogonal electrical field components exist in the direction of radiation which indicates that this antenna owns a dual-polarization characteristic. The technologies of the stair-like ground plane and loading additional structures are utilized to improve the impedance bandwidth to 72.4% (1.48 to 3.16 GHz) for VP and 46% (1.69 to 2.7 GHz) for HP. By adjusting the size of the large ground, the dual-polarized port isolation can be enhanced to 40–60 dB, and the gains in operating band can be stable at a higher value of 4 dBi. Moreover, the low-profile height of 79.5 mm is attained through the CST software's optimizer. The analysis of surface current distributions and the equivalent current antenna array radiation model are adopted in this paper to interpret the mechanism of the antenna. The detailed antenna structure is presented in Section 2; simulation and analysis are depicted in Section 3; experimental results are shown in Section 4; the characteristics of this antenna are analyzed in Section 5, while the conclusions are provided in Section 6.

## 2. ANTENNA GEOMETRY

The geometry of the proposed antenna is shown in Figure 1. The proposed dual-polarized antenna consists of a VP element and an HP element. As shown in Figure 1(b), VP element is a modified low-profile monopole with a top-loading metal disk shorted to the stair-like ground plane by four equally-spaced metallic pins. This structure of a four-metal-pins shorted patch has been widely utilized for a low-profile monopole [3, 4, 14, 18–23]. However, we have made a modification by mounting four-opening pins on the ground plane, which is able to compensate the reactance for bandwidth improvement. The stair of the ground, which is used for achieving wide impedance bandwidth, is mainly a metallic tube with the inner diameter equal to the diameter of the feeding coaxial cable's outer conductor. In addition, the inner conductor of the feeding cable passes through the metal tube and then connects with the top-loading patch. Other similar techniques to feed patches crossing other layers have been proposed for multi-feed antennas [24]. Based on the conventional monopole, we load a metal patch on the top and apply a ground-plane, by which the length of current's path is increased, thereby reducing the profile height effectively.

The HP element is a printed antenna shown in Figure 1(c), whose radiators and feeding network are printed on both sides of an F4B substrate ($\varepsilon_r = 3$ and thickness = 2 mm). The radiators are

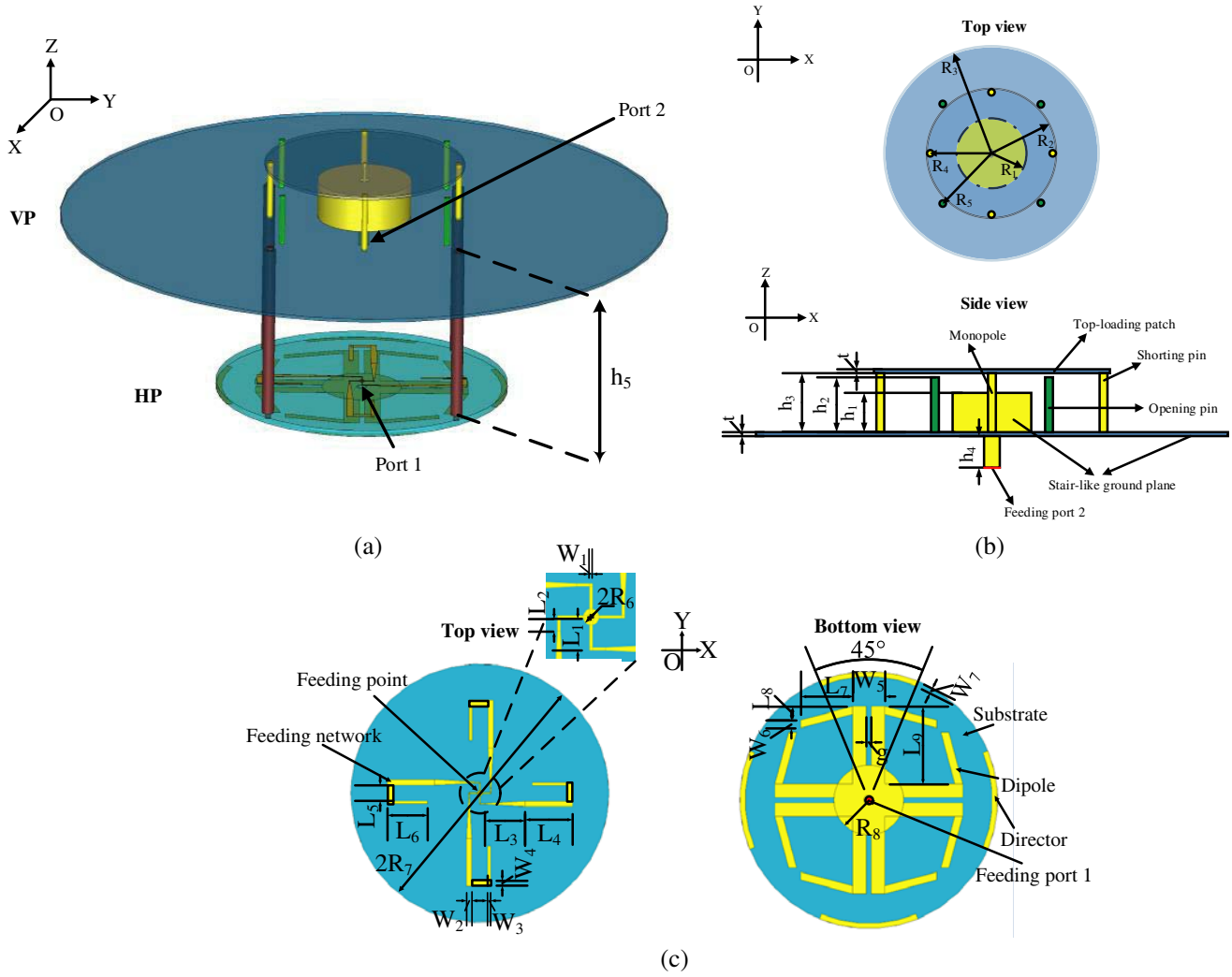


**Figure 1.** Geometry of the proposed antenna. (a) Perspective view. (b) VP element. (c) HP element.

four directional antennas radiating toward four directions $(\pm x, \pm y)$, respectively, and each directional antenna is made by a dipole loaded with a parasitic strip. The parasitical element, served as a director, is able to improve the gain in azimuth plane, extend the bandwidth, and also reduce the out-of-roundness. Here an especially designed four-way printed power divider is used as the feeding network to provide signals with equal amplitude and phase. This four-way printed power divider consists of four broadband baluns, which has been widely used in [14, 16–18, 23, 25–27], and an impedance matching circuit. At the center of the antenna element, the four branches of power divider should be connected to a $50\,\Omega$ feeding coaxial line, thus the impedance of each branch at this point should be equal to $200\,\Omega$ for parallel connection, whereas the balun should have a impedance of $70\,\Omega$ to match the impedance with the dipole. Therefore, to satisfy the matching requirement, we design a matching circuit for connecting four shunt broadband baluns to feeding point through four tapered transformers, which is helpful in increasing the impedance bandwidth. By positioning the HP element below the large ground of VP antenna element with an optimum distance of 57 mm, an enhancement of the isolation can be achieved. It should be noted that the final optimum geometric parameters applied to achieve broadband, high gain, and omnidirectional radiation patterns are pursued for the proposed antenna, and the description of optimization procedure, such as multi-objective optimization of a single element antenna, has already been proposed in [28]. The detailed values of parameters of the proposed antenna are optimized by CST software and listed in Table 1.

**Table 1.** Geometric parameters optimized for the proposed antenna (Unit: mm).

| Parameter | Value | Parameter | Value | Parameter | Value | Parameter | Value |
|---|---|---|---|---|---|---|---|
| $R_1$ | 15.4 | $h_1$ | 12.5 | $W_4$ | 2 | $L_5$ | 5.85 |
| $R_2$ | 33 | $h_2$ | 16.5 | $W_5$ | 12 | $L_6$ | 15 |
| $R_3$ | 100 | $h_3$ | 17.5 | $W_6$ | 3 | $L_7$ | 19.32 |
| $R_4$ | 31 | $h_4$ | 9 | $W_7$ | 2 | $L_8$ | 5.18 |
| $R_5$ | 38.3 | $h_5$ | 57 | $L_1$ | 4 | $L_9$ | 29 |
| $R_6$ | 1 | $W_1$ | 0.4 | $L_2$ | 1.6 | $t$ | 1 |
| $R_7$ | 48 | $W_2$ | 2 | $L_3$ | 15 | $g$ | 1.8 |
| $R_8$ | 13 | $W_3$ | 1.2 | $L_4$ | 17.7 | | |

## 3. SIMULATIONS AND ANALYSIS

### 3.1. VP Antenna

As displayed in Figure 1, VP antenna is a loaded monopole with stair-like ground plane. Simulating the antenna in CST Microwave Studio® produces the results shown in Figure 2. It can be seen from Figure 2(a) that the antenna impedance bandwidth with $|S_{11}| < -10$ dB is extremely wide with 75.6% covering 1.4–3 GHz, and the gain varies smoothly from 3.67 to 4.77 dBi in the whole operating frequencies. The normalized radiation patterns at 1.7, 2.2, and 2.7 GHz are illustrated in Figure 2(b),

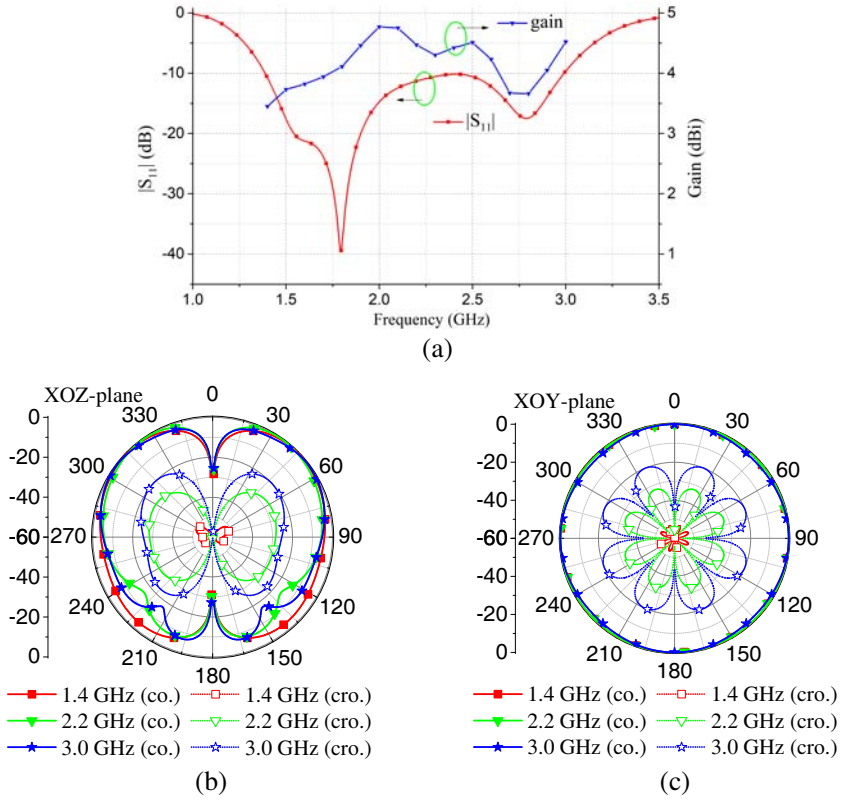


**Figure 2.** Simulated results of the proposed VP antenna. (a) $|S_{11}|$ and gains. (b) $XOZ$-plane normalized radiation patterns. (c) $XOY$-plane normalized radiation patterns.

which can reveal the patterns, in azimuth plane, are omnidirectional with the out-of-roundness less than 2 dB. Because of the reflection of its large ground plane, some up tiles of the maximum radiation directions are generated in elevation plane. In terms of the configurable dimensions, this antenna has a size quite small on the polarized direction which is only 0.095 $\lambda_L$ at the lowest operating frequency.

### *3.1.1. Radiation Mechanism Analysis*

To understand the radiation mechanism of the VP antenna, the surface current of VP antenna is simulated. Figure 3 shows the simulated surface current distributions at 1.7 GHz and 2.7 GHz. As seen, at the lower frequency, the current mainly distributes on the shorting pins, the side wall of the stair-like ground, and the feeding inner conductor above the ground, whereas unlike the occasion at the lower frequency, the current of the higher frequency is not mainly on the shorting pins, while large amount of current appeares on the opening pins. This is because the current at the lower frequency looks for resonant structures owning relative long current pathes to radiate, and the shorting pins connecting with the top patch can form long pathes; therefore, they act as the main radiators. However, at the higher frequency, the pathes for resonance are shrunk, thus the shorting and opening pins can all be used as the key radiators. For the top-loading patch and stair-like ground plane, they are just applied to transmit the current and not used for the VP radiation. In addition, the current distributions are mainly on the under surface of the top patch and the upper surface of this ground plane.

In order to further analyze above phenomenon, the simulated phase values of the current at 1.7 GHz and 2.7 GHz are extracted. Because of central symmetry of VP antenna, one radius cross-section is selected to simulate, and then the comparisons between the lengths of different structures (termed as AB-HI) and corresponding phase values are plotted in Figure 4. We can judge the current pattern of each structure in Figure 4 according to the slow-wave coefficient formula as depicted in [29]:

$$\zeta = \frac{\beta}{k} = \frac{\Delta\phi}{\Delta\phi_0} \tag{1}$$

where $\zeta$ is the slow-wave coefficient; $\beta$ is the phase constant; $k$ is the wave number in free space; $\Delta\phi$ is the phase shift; and $\Delta\phi_0$ is the corresponding one in free space. When $\zeta \geq 1$, the current is in traveling

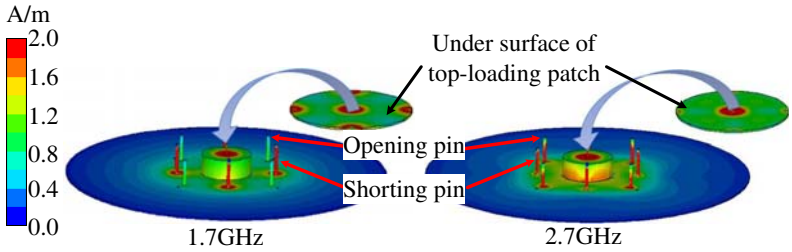


**Figure 3.** Surface current distribution of VP antenna.

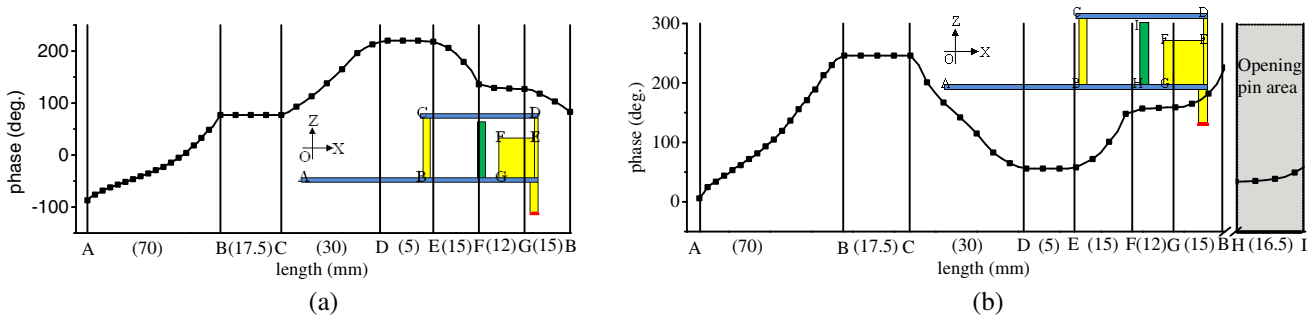


**Figure 4.** Comparisons between the lengths of different structures and corresponding phase values. (a) 1.7 GHz. (b) 2.7 GHz.

**Table 2.** Parameters' values of Equation (1) and the current pattern for different structures.

| Frequency | Parameter | AB | BC | CD | DE | EF | FG | GB | HI |
|---|---|---|---|---|---|---|---|---|---|
| 1.7 GHz | $\Delta\phi$ | 164° | 0° | 143° | 2° | 82° | 9° | 44° | - |
| | $\Delta\phi_0$ | 142.8° | 35.6° | 61.2° | 10.2° | 30.6° | 24.5° | 30.6° | - |
| | $\zeta$ | 1.15 | 0 | 2.34 | 0.19 | 2.68 | 0.37 | 1.44 | - |
| | CP | TW | SW | TW | SW | TW | SW | TW | - |
| 2.7 GHz | $\Delta\phi$ | 240° | 0° | 190° | 0° | 94° | 9° | 67° | 25° |
| | $\Delta\phi_0$ | 226.8° | 56.7° | 97.2° | 16.2° | 48.6° | 38.9° | 48.6° | 53.5° |
| | $\zeta$ | 1.06 | 0 | 1.95 | 0 | 1.93 | 0.23 | 1.38 | 0.47 |
| | CP | TW | SW | TW | SW | TW | SW | TW | SW |

*CP — Current Pattern, TW — Traveling Wave, SW — Standing Wave.

wave pattern, and when $\zeta \approx 0$, the current is in standing wave pattern. The parameters' values of Equation (1) and the current pattern for the different structures are listed in Table 2. It can be found that both at the lower frequency and higher frequency, the current patterns of the vertical structures are all standing waves, which means that they are served as main radiators for resonance. However, the current distributions on other horizontal structures include top patch and stair-like ground plane which have large radiating areas all exhibiting traveling wave patterns, and because of the property of flowing radiation, the traveling wave's reflection is relatively small, hence this antenna constructed by the horizontal structures displays a good impedance matching provided by the small reflections; in other words, the wideband characteristic of the proposed VP antenna can be achieved.

### *3.1.2. Operating Frequencies Analysis*

As shown in Figure 2(a), two resonant frequencies are available to generate stagger tuning for attaining broadband. Moreover, as mentioned in the above analysis, the lower resonant frequency is determined by the structure with a long size. Therefore, we take the loop form by CD, DE, EF, FG, GB, BC in Figure 4 as an example and examine the relationship between the loop's circumference (termed as C) and the lower resonant frequency by the parameter sweep analysis of CD. Figure 5(a) shows the effect of changing CD length on the simulated $|S_{11}|$, and additionally, the corresponding results are listed in Table 3. It is observed that the increase of the C causes the resonant frequency ($f_{rL}$) shifting to lower band; however, the value of parameter C is always approximately corresponding to the electrical length of $0.56 \sim 0.57\ \lambda_{rL}$ at the resonant frequency. At higher frequencies, the opening pins with short sizes are served as the main radiators; therefore, we examine the relationship between the length of opening pins and the higher resonant frequency ($f_{rH}$) by the parameter sweep analysis of HI whose results are shown in Figure 5(b) and also list the results in Table 3. As seen, HI has a stable electrical length value of approximately $0.15 \sim 0.16\ \lambda_{rH}$. To sum up, the stable relationship between the structure's electrical lengths and resonant frequencies can be applied to this design of antenna.

**Table 3.** Parameters' values of C and HI.

| | Length | $f_{rL}$ | Electrical length | | Length | $f_{rH}$ | Electrical length |
|---|---|---|---|---|---|---|---|
| C | 90.5 mm | 1869 MHz | $0.56\lambda_{rL}$ | HI | 16 mm | 2788 MHz | $0.15\lambda_{rH}$ |
| | 92.5 mm | 1832 MHz | $0.57\lambda_{rL}$ | | 16.5 mm | 2760 MHz | $0.15\lambda_{rH}$ |
| | 94.5 mm | 1796 MHz | $0.57\lambda_{rL}$ | | 17 mm | 2737 MHz | $0.16\lambda_{rH}$ |
| | 96.5 mm | 1750 MHz | $0.56\lambda_{rL}$ | | 17.5 mm | 2712 MHz | $0.16\lambda_{rH}$ |

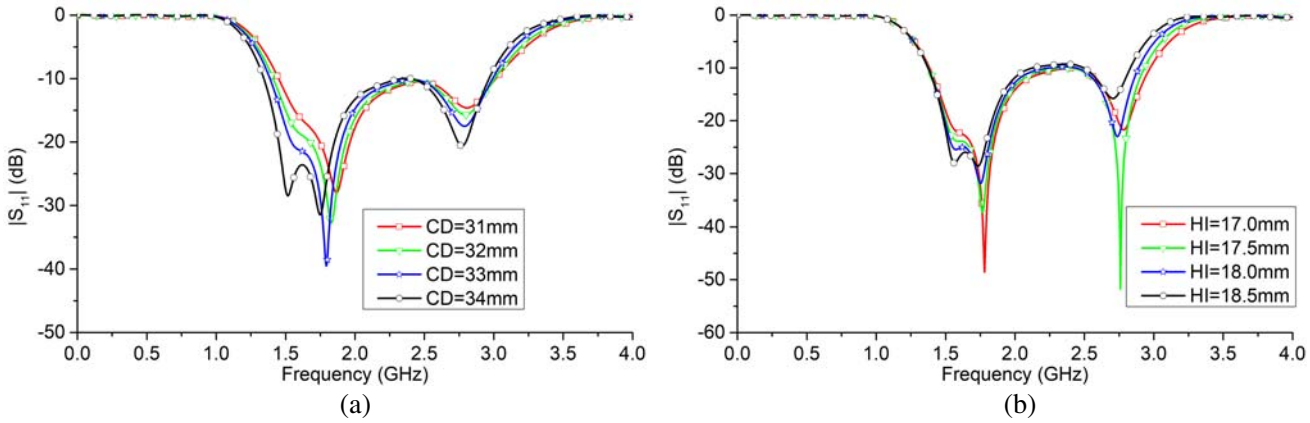


**Figure 5.** Reflection coefficient of VP antenna, (a) with different lengths of CD, (b) with different lengths of HI.

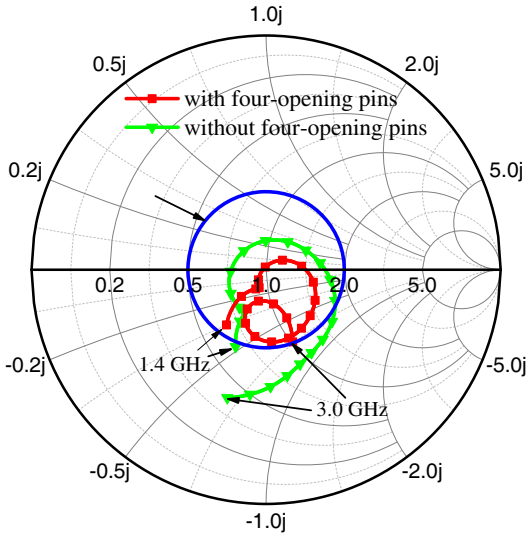


**Figure 6.** Impedance curves of VP antenna with/without four-opening pins on Smith chart.

### *3.1.3. Function Analysis of Metallic Pins*

Metallic pins are not only used for radiation, but also used to adjust the impedance matching. Because of similar heights, the shorting and opening cylinders can generate opposite property reactances for compensation. To study the contribution of four-opening pins, which are developed in this paper to improve antenna performance, we plot the impedance curves with/without four opening pins in Figure 6. It can be seen that with opening pins, the impedance curve moves into the $\Gamma = 1/3$ circle on the Smith chart indicating the amelioration of impedance matching; in other words, the bandwidth is broadened by them effectively.

## 3.2. HP Antenna

As shown in Figure 1(c), HP antenna is a combination of four concentrically arranged Yagi-Uda-like antennas. The simulated results of this antenna from CST software are depicted in Figure 7 including reflection coefficients, gains, and radiation patterns. It can be observed that the antenna's impedance bandwidth is broad of 49.9%, which covers 1.7 GHz–2.83 GHz, and the gains range from 1.2 dBi to 1.52 dBi, significantly lower than the VP's. This HP antenna also has omnidirectional patterns with

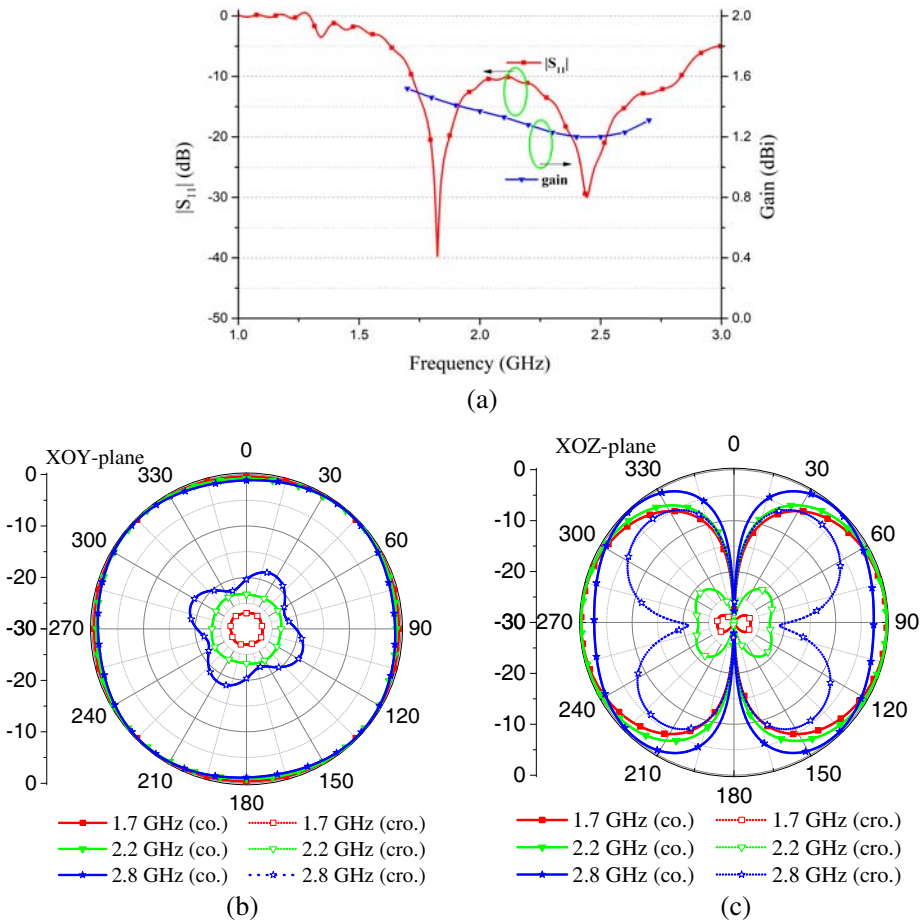


**Figure 7.** Simulated results of the proposed HP antenna. (a) $|S_{11}|$ and gains. (b) $XOY$-plane normalized radiation patterns. (c) $XOZ$-plane normalized radiation patterns.

the out-of-roundness less than 2 dB in the whole operating band.

### *3.2.1. Radiation Mechanism Analysis*

In order to explain the radiation mechanism of the HP element, we use equivalent current radiation model, as demonstrated in Figure 8, which applies linear superposition of all isolated radiation elements' field intensities based on their own surface current distributions to calculate the total far-field electric field intensity of the antenna, and as a result, each element is modeled as a dipole source. Taking any one of the four Yagi-Uda-like antennas as an example, it can be considered as a directional antenna composed of a fed-dipole and a parasitic segment, on which the current distributions are both assumed to be sinusoidal and expressed as follows:

$$I(z) = I_{\mathrm{m}} \sin\left[k(l - |z|)\right] \tag{2}$$

where $I_{\mathrm{m}}$ is the amplitude; $k = \frac{2\pi}{\lambda}$; $l$ is the length of the radiation element. Therefore, the current distribution of each radiation element generated by CST simulation software can be fitted with a sinusoid to solve the value of parameter $I_{\mathrm{m}}$. Figure 9 depicts the simulated amplitude and phase distribution curves and fitted sinusoid of all the elements at the HP antenna's resonance frequencies (1.8 and 2.4 GHz). It is clear that at the same frequency, the four directional antennas have the same current amplitude distributions, and due to the end effect generated by the charge accumulation at the antenna's terminations, the amplitude values at the ends of these elements should not be zero. In addition, we can observe from Figure 9 that the dipole's phase advances the parasitic element's for each Yagi-Uda-like antenna, thereby forming directional radiation.

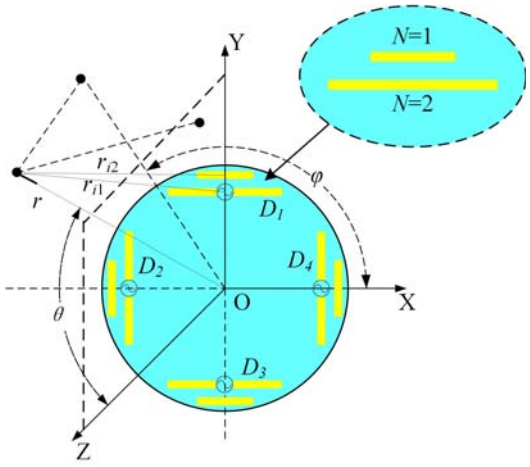


**Figure 8.** Equivalent current radiation model of the proposed HP antenna.

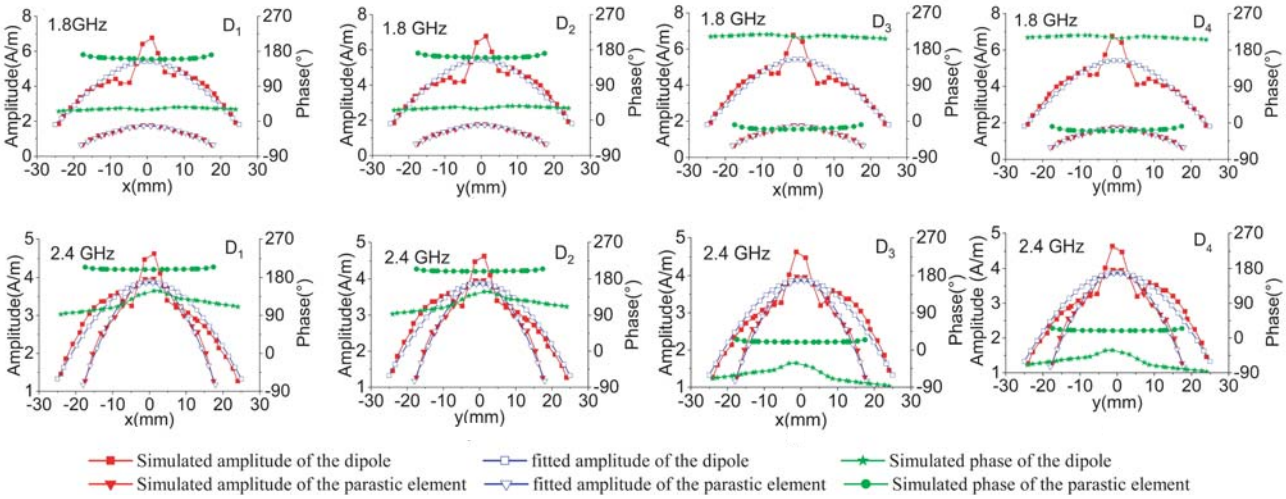


**Figure 9.** Simulated amplitude and phase values with fitted sinusoid of each element of HP antenna at resonance frequencies 1.8 GHz and 2.4 GHz.

According to fitted curves, the values of $I_{\mathrm{m}}$ of each element can be calculated. Because of the current standing wave pattern, the phase distribution along each element is approximately uniform. Table 4 lists the amplitude and phase values of the radiators, with which the HP antenna's patterns can be calculated through the following functions.

**Table 4.** Detailed amplitude and phase values of the radiators.

| Frequency | Element | Amplitude (A/m) | Phase of $D_1$ (°) | Phase of $D_2$ (°) | Phase of $D_3$ (°) | Phase of $D_4$ (°) |
|---|---|---|---|---|---|---|
| 1.8 GHz | Dipole | 3.011 | 31.74 | 31.74 | 211.75 | 211.75 |
| | Parasitic element | 1.52 | 162.85 | 162.86 | −17.15 | −17.14 |
| 2.4 GHz | Dipole | 4.328 | 120.38 | 117.81 | −62.39 | −62.39 |
| | Parasitic element | 6.4 | 200.07 | 200.39 | 20.37 | 20.39 |

In terms of a single radiation element, the field intensity created by the current that satisfies $I(z) = I_{\mathrm{m}} \sin[\beta(l - |z|)]$ is

$$E_\theta = j\frac{60I_m}{\lambda r} f(\theta, \varphi) e^{-jkr} \tag{3}$$

Thus, for a Yagi-Uda-like antenna $D_i$ $(i = 1, 2, 3, 4)$, the entire far-field intensity is the linear superposition of $E$-dipole and E-director, based on the interference principle of field, and can be expressed as follows:

$$\begin{aligned} E_i &= E_{i1} + E_{i2} \\ &= \frac{60I_{i1}e^{j\xi_{i1}}}{r_{i1}} f_{i1}(\theta, \varphi) e^{-jk_0 r_{i1}} + \frac{60I_{i2}e^{j\xi_{i2}}}{r_{i2}} f_{i2}(\theta, \varphi) e^{-jk_0 r_{i2}} \end{aligned} \tag{4}$$

where $I_{iN}$ is the maximum current magnitude; $\xi_{iN}$ is the current standing wave phase; $k_0$ is the wave number in free space; $r_{iN}$ is the distance from the center point on the source to the observation point $M$. $N = 1$ represents the dipole of $D_i$; $N = 2$ represents the director of $D_i$. $f_{iN}(\theta, \varphi)$ is the direction function of an isolated radiator and can be written as follows:

$$f_{iN}(\theta, \varphi) = f_{iN}(\Theta) = \frac{\cos(kl_N \cos\Theta_i) - \cos kl_N}{\sin\Theta_i} \tag{5}$$

where $\Theta_i$ is the angle from the observation direction OM to the axis along the element $D_i$; $\cos\Theta_{1,3} = \sin\theta\cos\varphi$; $\cos\Theta_{2,4} = \sin\theta\sin\varphi$; $l_N$ is the half length of the element. Finally, according to the interference principle of field, the total far-field intensity of the HP antenna can be derived as

$$\begin{aligned} E_M &= E_1 + E_2 + E_3 + E_4 = E_M(\theta, \varphi) \\ &= \left[ \left| (E_1 + E_3)\sin\varphi + (E_2 + E_4)\cos\varphi \right|^2 + \left| (E_1 + E_3)\cos\varphi + (E_2 + E_4)\sin\varphi \right|^2 \right]^{\frac{1}{2}} \end{aligned} \tag{6}$$

The normalized direction function is

$$F(\theta, \varphi) = \frac{|E_M(\theta, \varphi)|}{|E_M(\theta, \varphi)|_{\max}} \tag{7}$$

To further validate the equivalent current radiation model, the comparison between the simulated and calculated normalized patterns in the $XOY$-plane and $XOZ$-plane at different resonance frequencies is provided in Figure 10. Note that the two methods' results coincide well with each other, and the antenna realizes omnidirectional radiation in horizontal plane. However, the radiation gain of the antenna is relatively low. This is because each directional antenna possesses a powerful backward radiation as

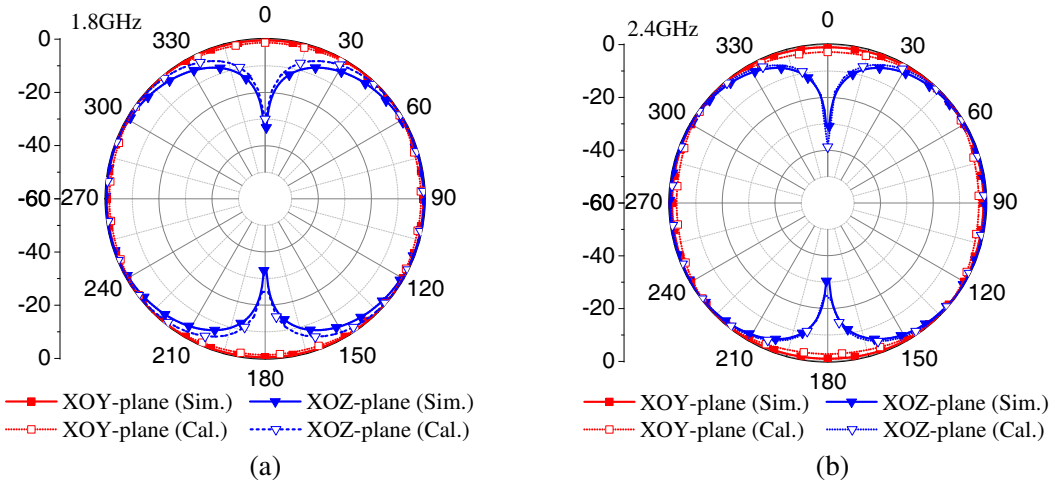


**Figure 10.** Comparison between the simulated and calculated normalized antenna patterns. (a) 1.8 GHz. (b) 2.4 GHz.

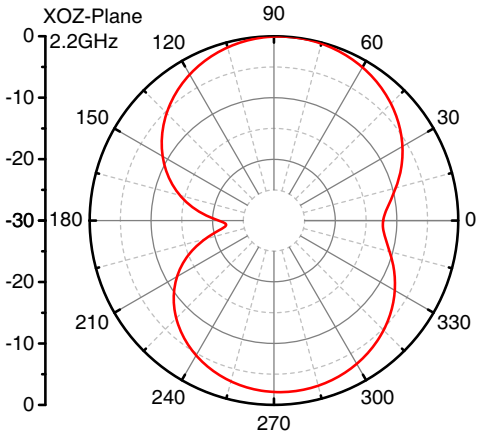


**Figure 11.** Radiation pattern in $XOZ$-plane of a single directional antenna applied for HP antenna at 2.2 GHz.

shown in Figure 11. Take $+y$ direction as an example, the forward radiation of $D_1$ interferes the backward radiation of $D_3$. In addition, due to the long distance between them, the in-phase interference along $+y$ direction may not be generated in normal conditions, resulting in the reduction of the radiation field intensity. For example, at 2.2 GHz, $D_1$ is departed away from $D_3$ with 77 mm, and the phase shift of 6.42 rad (368°) is acquired, in which case the field of $D_1$ is weakened by $D_3$ in $+y$ direction.

It needs to be emphasized that the current distributions of the crossed dipoles [30] in the equivalent current radiation model are the results simulated by CST software, and then the co-polarized radiation field and patterns are calculated by combining the results with the discrete arrays model.

### *3.2.2. Operating Frequencies Analysis*

$D_i$ is a Yagi-Uda like antenna with a dual-resonance structure. To better explain this performance, Figure 12 gives the relationship between surface current amplitudes and frequencies of the dipole and parasitic element for $D_i$. It can be observed that the first resonance frequencies of the current on the fed dipole and parasitic segment are 1.7 GHz and 2.8 GHz, respectively, and due to the effect of stagger tuning, the operating band of $D_i$ covers 1.7–2.8 GHz, thereby achieving broad bandwidth.

For the entire HP antenna, the lower and higher resonant frequencies (1.8 GHz and 2.4 GHz) are also determined by the dipole's length and parasitic segment's length, respectively. Considering the effect of

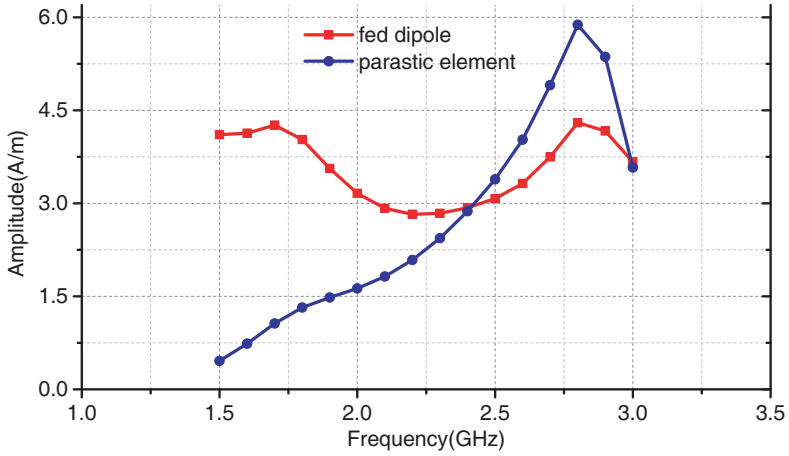


**Figure 12.** Relationship between surface current amplitudes and frequencies of the dipole and parasitic element for $D_i$.

the substrate, the wavelength $\lambda_e$ in the substrate is equal to $\frac{\lambda_0}{\sqrt{\varepsilon_e}}$ and should satisfy $\frac{\lambda_0}{\sqrt{\varepsilon_r}} < \lambda_e < \lambda_0$. The dipole's length is 52 mm, and $\lambda_e$ at the 1.8 GHz is in the range from 96.34 to 166.67 mm; therefore, the dipole's length corresponds to $\frac{\lambda_e}{2}$. The parasitic segment's length is 37.68 mm, and $\lambda_e$ at 2.4 GHz is in the range from 72.25 to 125 mm, hence its length corresponds to $\frac{\lambda_e}{2}$, as well. Consequently, according to the relationship between the resonant frequencies and the radiators' electrical length of $\frac{\lambda_e}{2}$, we can design this antenna.

### 3.3. Dual-Polarized Antenna

There are two scenarios for the position of VP and HP elements to assemble a dual-polarized antenna. The first one is placing the HP element above the VP antenna, and the other is the inverted position which is adopted in this paper to attain higher isolation as plotted in Figure 1(a). Since the diameter of the ground of VP element is 2.2 times of that of HP element, the electromagnetic energy coupling between VP and HP antennas is isolated effectively. In addition, in this proposed antenna, the respective radiators for VP and HP are strictly orthogonally positioned, thus the coupling between VP and HP antennas is weak, which achieves good isolations. The port isolations of the two scenarios, when the spacings between the two elements are both 57 mm, as shown in Figure 13, verifies that positioning HP antenna beneath VP antenna achieves better performance of 40–50 dB isolations, and at the same time, the large ground plane of VP element can also cause significant influence on the radiation of HP element. The simulated results, including reflection coefficients, gains, and radiation patterns, are demonstrated in Figure 14 and 15. It can be noted that the antenna's impedance bandwidths are 75.6% (1.4–3.1 GHz) for VP and 50.1% (1.68 GHz–2.83 GHz) for HP, and the gains range from 3.48 dBi to 4.86 dBi for VP and 3.55 dBi to 4.17 dBi for HP. This assembled antenna has omnidirectional patterns with the out-of-roundness less than 2 dB in the whole operating band. Compared with the separation of the two antenna elements, the combination brings nearly no change about the reflection coefficients, VP antenna's gains, and radiation patterns. Nevertheless, due to the reflection of the large ground plane, the direction of maximum radiation for the HP antenna is down tilt by approximately 45°, and the gains are also enhanced by approximately 2.5 dB.

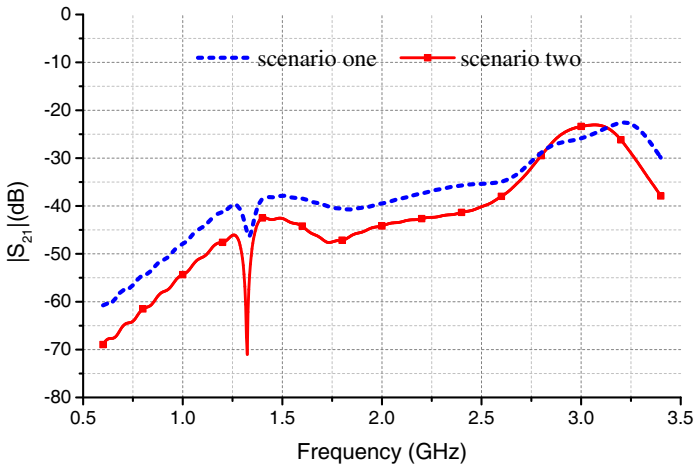


**Figure 13.** Two ports simulated isolations for two different positions.

To illustrate the effects of the ground on the HP element, image theory is applied to form the HP element's direction function of the dual-polarized antenna. Through multiplying the separated HP antenna's direction function in Eq. (7) by the corresponding array factor of a two-elements array with constant amplitude and out of phase, the formula of the HP element's normalized direction function can be given by

$$F_{HP}(\theta,\varphi) = \frac{|E_M(\theta,\varphi)|}{|E_M(\theta,\varphi)|_{\max}} |\sin(k_0 H\cos\theta)| \tag{8}$$

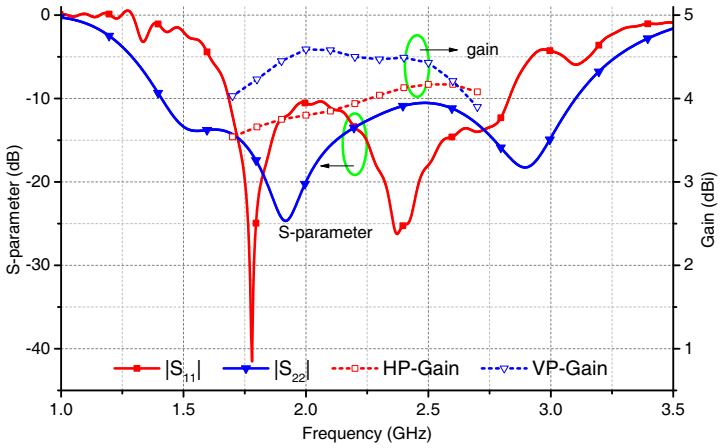


**Figure 14.** Simulated reflection coefficients and gains of dual-polarized antenna.

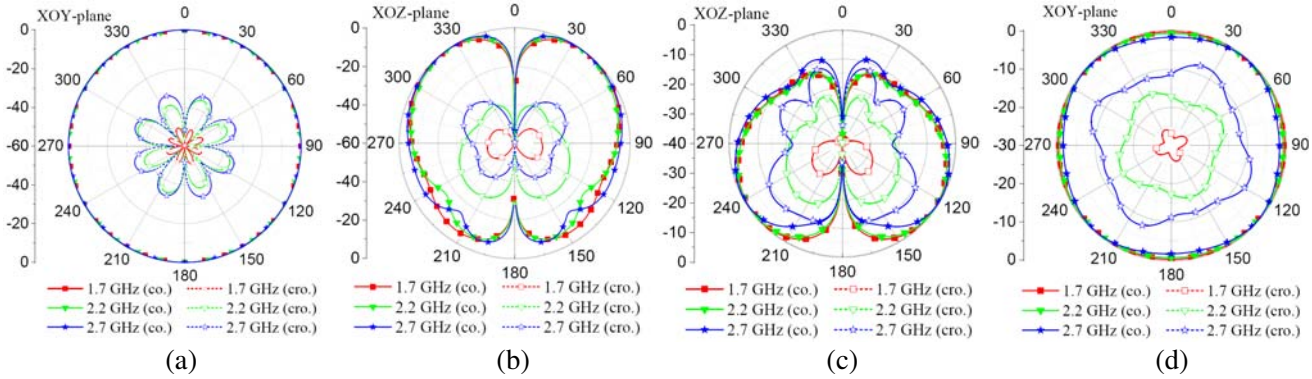


**Figure 15.** Simulated normalized radiation patterns of dual-polarized antenna. (a) $XOY$-plane for VP. (b) $XOZ$-plane for VP. (c) $XOZ$-plane for HP. (d) $XOY$-plane for HP.

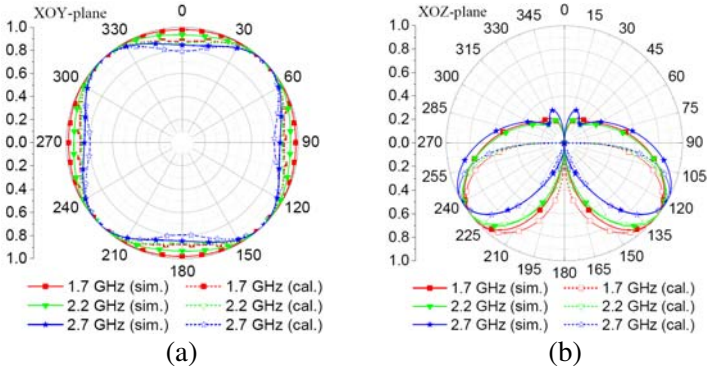


**Figure 16.** Comparison between the simulated and calculated linear radiation patterns of HP element. (a) $XOY$-plane. (b) $XOZ$-plane.

where $H$ equal to $h_5$ (57 mm) is the distance from the HP antenna to the ground of VP element. In Figure 16, the simulated linear radiation patterns of HP element are compared with the ones calculated through function in Eq. (8). We observe from Figure 16 that the calculated and simulated patterns' main lobes coincide well with each other. The array effect generated by the large ground of VP element may create enhancement of gains of HP element, which can be proved by the calculation of gain function.

The gain function is expressed as

$$G = D\eta = \frac{4\pi}{\int_0^{2\pi}\int_0^{\pi} F^2(\theta,\varphi)\sin\theta d\theta d\varphi} \tag{9}$$

And applying Eq. (8) into Eq. (9), we can obtain the HP antenna's calculated gains in the operating band of 1.68–2.83 GHz. The simulated and calculated gains with slight discrepancy are shown in Figure 17, which are all larger than the gains in the separated HP antenna.

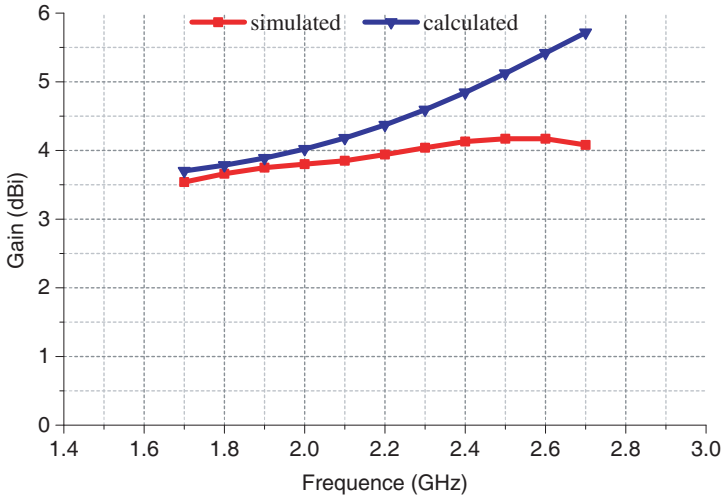


**Figure 17.** Comparison between the simulated and calculated peak gains of HP element.

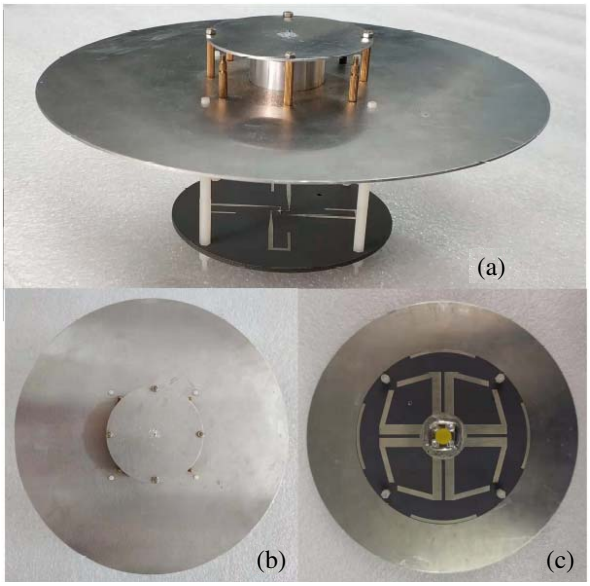


**Figure 18.** Photograph of the proposed antenna. (a) 3-D view. (b) Top view. (c) Bottom view.

## 4. MEASURED RESULTS AND ANALYSIS

The simulated results illustrate that the proposed antenna can realize high isolation low-profile dual-polarized, and broadband performance. Moreover, the calculated consequences based on the surface

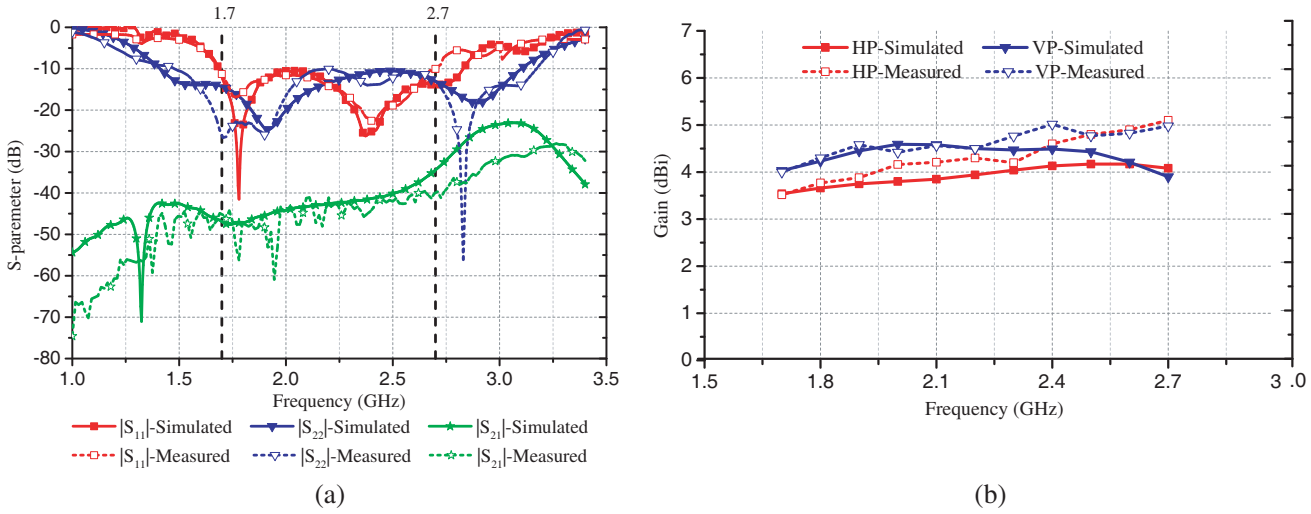


**Figure 19.** Comparison between the simulated and experimental results of the proposed dual-polarized antenna. (a) *S*-parameters. (b) Gains.

**Table 5.** Comparison between the proposed antenna and other antennas.

| Antenna Type | Bandwidth for VP | Bandwidth for HP | Profile Height | Isolation | Gains |
|---|---|---|---|---|---|
| The Antenna in [12] | 17.4% (0.806–0.96 GHz) | 35% (1.8–2.7 GHz) | 110 mm | 25–30 dB | Around 1.5 dBi in lower band<br>Around 4.5 dBi in higher band |
| The Antenna in [13] | 137% (0.671–3.58 GHz) | 55% (1.7–3 GHz) | 102.6 mm | More than 25 dB | Less than 3.9 dBi |
| The Antenna in [14] | 152% (0.82–6 GHz) | 63% (1.53–2.95 GHz) | 97.5 mm | More than 31 dB | 2.3 to 4.9 dBi for HP<br>2 to 4.7 dBi for VP |
| The Antenna in [15] | 45.5% (1.7–2.7 GHz) | 45.5% (1.7–2.7 GHz) | 30.6 mm | More than 20 dB | 3.8 to 5.5 dBi for HP<br>2.7 to 6.3 dBi for VP |
| The Antenna in [16] | 24% (770–980 MHz)<br>75.2% (1.7–3.75 GHz) | 39.5% (690 MHz–1.03 GHz)<br>62% (1.69–3.21 GHz) | 117.5 mm | 14 dB in 0.69–1.03 GHz<br>More than 25 dB in 1.69–3.75 GHz | 3.8 to 5.5 dBi for HP<br>2.7 to 6.3 dBi for VP |
| The Antenna in [17] | 128% (0.7–3.2 GHz) | 39.6% (0.77–1.15 GHz)<br>55.3% (1.66–2.93 GHz) | Larger than 100 mm | Higher than 20 dB | 3.8 to 5.5 dBi for HP<br>2.7 to 6.3 dBi for VP |
| The Antenna in [18] | 25% (1.7–2.2 GHz) | 25% (1.7–2.2 GHz) | 72 mm for a single element | Around 40 dB | Element:<br>Less than 1.5 dBi for HP<br>Less than 2.5 dBi for VP<br>Array:8 dBi. |
| The Proposed Antenna | 72.4% (1.48–3.16 GHz) | 46% (1.69–2.7 GHz) | 79 mm | 40-60 dB | around 4 dBi |

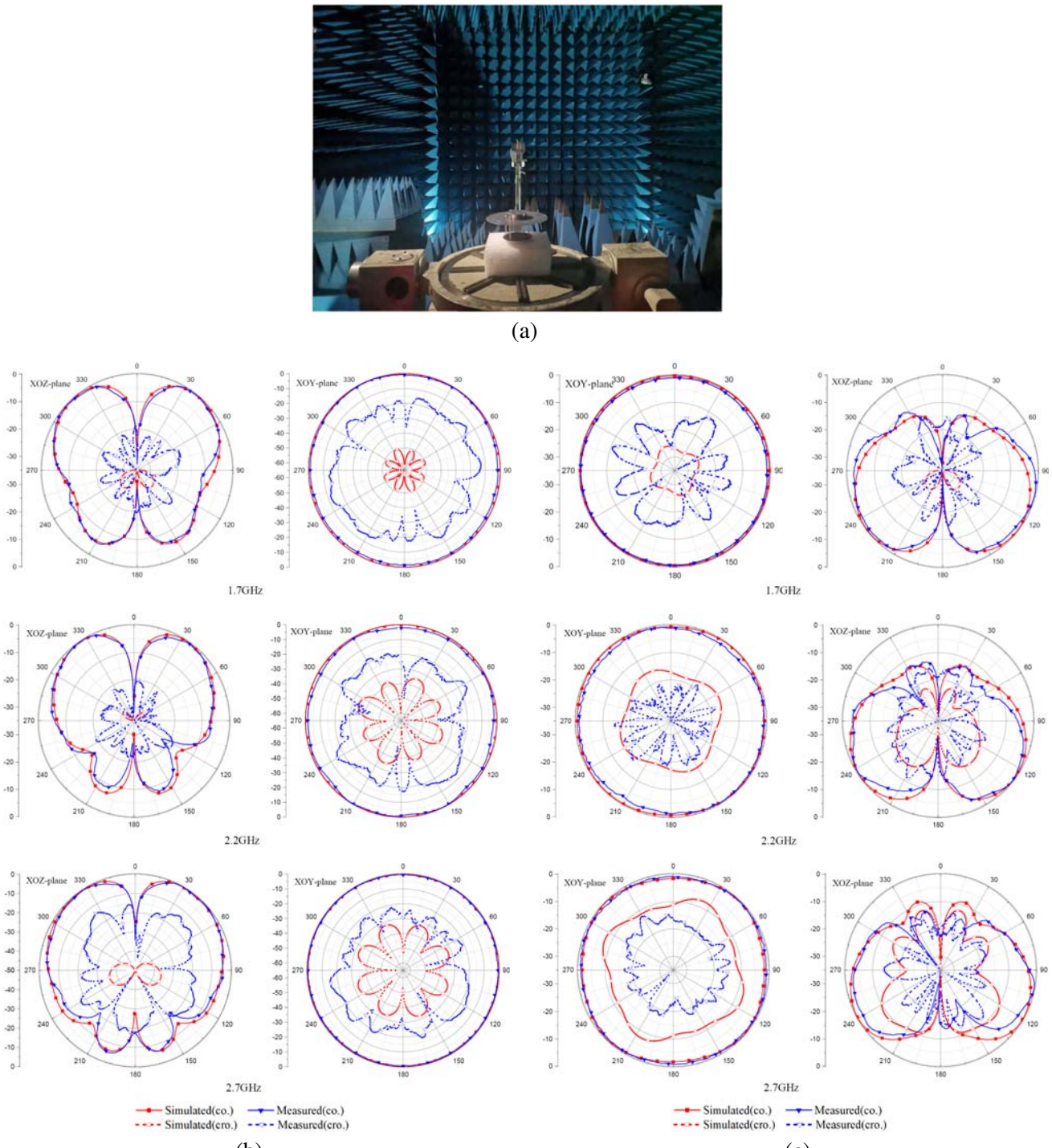


**Figure 20.** (a) Measured environment of the proposed antenna and simulated and measured radiation patterns of (b) VP element. (c) HP element.

current distributions agree well with the simulated ones. A prototype has been manufactured to validate the antenna design, as shown in Figure 18. Both VP and HP elements use 50 Ω SMAs to connect the feeding coaxial lines. This antenna has been measured in an anechoic chamber by the Agilent N5227A vector network analyser, and its simulated and measured results, including $S$-parameters, gains, and normalized antenna patterns, are described in Figures 19 and 20. Furthermore, the measurement

**Table 6.** Analysis for each antenna's characteristics.

| Antenna Type | Analysis for Characteristics |
|---|---|
| The Antenna in [12] | Narrow bandwidth caused by the elements' structures; Low isolation attributed to the too close distance between two elements; High profile. |
| The Antenna in [13] | Wide bandwidth affected by impedance transformation of feeding network; High profile and low isolation caused by elements' relative position. |
| The Antenna in [14] | Wide bandwidth affected by elements' structures; High profile and also high isolation attributed to elements' relative position. |
| The Antenna in [15] | Wide bandwidth affected by impedance transformation of feeding network; Low profile affected by the AMC, however, low isolation due to low profile. |
| The Antenna in [16] | Wide bandwidth and multiple bands affected by the elements' structures and the balun, but low isolation caused by the multi-elements' relative positions. |
| The Antenna in [17] | Wide bandwidth and multiple bands affected by the elements' structures and the balun, but low isolation caused by the multi-elements' relative positions. |
| The Antenna in [18] | Narrow bandwidth and low gains caused by the elements' structures, but high isolation affected by the relative positions of the polarized elements; Eight-element array for higher gains. |
| The Proposed Antenna | Wide bandwidth, low-profile and high isolation achieved by broadband elements, broadband balun included tapered transformers and reasonable relative position between the elements. |

environment of the proposed antenna is displayed in Figure 20(a). The 10 dB impedance bandwidths of the VP and HP elements are 1.48–3.16 GHz and 1.69–2.7 GHz, respectively. The isolation between two ports is higher than 40 dB. The measured gains are also stable at 4 dBi. The radiation shows omnidirectional patterns in horizontal plane with out-of-roundness less than 2 dB. Finally, the measured results coincide well with the simulated ones, and the slight discrepancies are caused by the effect of the experiment environment, loss of feeding lines, and fabrication errors.

## 5. THE CHARACTERISTICS OF THE PROPOSED ANTENNA

The comparisons between the proposed antenna and other antennas are listed in Table 5, and the analysis for each antenna's characteristics is also introduced in this section as shown in Table 6. It is clear that our antenna has many merits, such as broadband, high isolation, and relatively stable gains.

## 6. CONCLUSION

A low profile, high isolation, broadband, dual-polarized omnidirectional antenna has been designed, fabricated, measured, and analyzed. This proposed design allows the antenna to display good performance such as the broad relative bandwidths of 72.4% and 46% for VP element and HP element, respectively, the omnidirectional radiation patterns with out-of-roundness less than 2 dB, the gains stable at 4 dBi, and the high isolations which are more than 40 dB. Through the CST software, we have obtained the antenna's electric parameters and then explained the impedance and radiation mechanism well by using the achieved surface current amplitudes and phases. This research can be extended to a wider antenna design field. In addition, this designed antenna is easy to form an array, and due to the operating band covering 1.7 to 2.7 GHz, it can be utilized in 4G communication systems.

## ACKNOWLEDGMENT

This work was supported in part by the Natural Science Foundation of Heilongjiang Province under Grant F2017011. The authors would also like to thank CST Ltd. Germany, for providing the CST Training Center (Northeast China Region) at our university with a free package of CST MWS software.

## REFERENCES

1. "Technical specification group radio access network; evolved universal terrestrial radio access (E-UTRA); base station (BS) radio transmission and reception," version (release 9) Third Generation Partnership Project(3GPP); TS 36.104 V12.7.0; 2015. *IEEE Transactions on Antennas and Propagation*, Vol. 66, No. 1, 81–87, 2017.
2. Yu, L., J. D. Song, Y. Gao, K. He, and F. Gao, "Low-profile dual-polarized omnidirectional antenna for broadband indoor distributed antenna system," *Progress In Electromagnetics Research Letters*, Vol. 67, 39–45, 2017.
3. Zhang, Y. W., S. Lin, S. Yu, S. L. Liu, G. J. Liu, and A. Denisov, "A dual-polarized omnidirectional antenna with two kinds of printed wideband low-profile radiating elements," *Progress In Electromagnetics Research Letters*, Vol. 80, 149–157, 2018.
4. Bai, X., M. Su, Z. D. Gao, and Y. A. Liu, "Broadband dual-polarized omnidirectional antenna based on magnetic dipoles," *IEICE Electronics Express*, Vol. 15, No. 5, 1–8, 2018.
5. Bhadoria, B. and S. Kumar, "A novel omnidirectional triangular patch antenna array using Dolph-Chebyshev current distribution for C-band applications," *Progress In Electromagnetics Research M*, Vol. 71, 75–84, 2018.
6. Puente, C., C. Borja, A. Teillet, D. Kirchoffer, and J. Anguera, "Slim triple band antenna array for cellular base stations," US Patent 8,497,814.
7. Barba, M., "A high-isolation, wideband and dual-linear polarization patch antenna," *IEEE Trans. Antennas Propag.*, Vol. 56, No. 5, 1472–1476, 2008.
8. Koohestani, M., A. A. Moreira, A. K. Skrivervik, and A. M. Kasgari, "A novel compact CPW-fed polarization diversity ultrawideband antenna," *IEEE Antennas Wireless Propag. Lett.*, Vol. 13, No. 13, 563–566, 2014.
9. Pattnaik, S., S. S. Behera, and S. Sahu, "Design of a new compact UWB polarization diversity antenna with stepped CPW-feed," *India Conf.*, 1–4, 2016.
10. Chacko, B. P., G. Augustin, and T. A. Denidni, "Electronically reconfigurable uniplanar antenna with polarization diversity for cognitive radio applications," *IEEE Antennas Wireless Propag. Lett.*, Vol. 14, 213–216, 2015.
11. Yahya, R., A. Nakamura, M. Itami, and T. A. Denidni, "A novel UWB FSS-based polarization diversity antenna," *IEEE Antennas Wireless Propag. Lett.*, Vol. 16, No. 1, 2525–2528, 2017.
12. Dai, X. W., Z. Y. Wang, C. H. Liang, X. Chen, and L. T. Wang, "Multiband and dual-polarized omnidirectional antenna for 2G/3G/LTE application," *IEEE Antennas Wireless Propag. Lett.*, Vol. 12, No. 3, 1492–1495, 2013.
13. Jolani, F., Y. Yu, and Z. Chen, "A novel broadband omnidirectional dual polarized mimo antenna for 4G LTE applications," *Proc.Int. Wireless Symp.*, 1–4, 2014.
14. Huang, H., Y. Liu, and S. Gong, "Broadband dual-polarized omnidirectional antenna for 2G/3G/LTE/WiFi applications," *IEEE Antennas Wireless Propag. Lett.*, Vol. 15, 576–579, 2016.
15. Wu, J., S. Yang, Y. Chen, S. Qu, and Z. Nie, "A low profile dualpolarized wideband omnidirectional antenna based on AMC reflector," *IEEE Trans. Antennas Propag.*, Vol. 65, No. 1, 368–374, 2017.
16. Guo, D., K. He, Y. Zhang, and M. Song, "A multiband dual-polarized omnidirectional antenna for indoor wireless communication systems," *IEEE Antennas Wireless Propag. Lett.*, Vol. 16, No. 99, 290–293, 2017.
17. Zhao, Z. T., J. X. Lai, B. T. Feng, and C. Y. D. Sim, "A dual-polarized dual-Band antenna with high gain for 2G/3G/LTE indoor communications," *IEEE Access*, Vol. 6, 61622–61632, 2018.

18. Quan, X. L. and R. L. Li, "A broadband dual-polarized omnidirectional antenna for base stations," *IEEE Trans. Antennas Propag.*, Vol. 61, No. 2, 943–947, 2013.
19. Lai, J. W., C. L. Tang, S. T. Fang, and K. L. Wong, "Broadband lowprofile cylindrical monopole antenna for 1800 MHz operation," *Microw. Opt. Technol. Lett.*, Vol. 41, No. 1, 39–40, 2004.
20. Yang, S. L. S. and K. M. Luk, "Design of a wide-band L-probe patch antenna for pattern reconfiguration or diversity applications," *IEEE Trans. Antennas Propag.*, Vol. 52, No. 4, 433–438, 2006.
21. Yi, L. P., G. S. Lamba, A. Gupta, and E. K. N. Yung, "A small omnidirectional patch antenna with ultra wide impedance bandwidth," *Microwave Conference, 2008, APMC 2008, Asia-Pacific.*, 1–4, 2008.
22. Wu, W., Y. Yin, Y. Zhao, and S. Zuo, "A miniaturized low-profile antenna for WLAN communications," *Microw. Opt. Technol. Lett.*, Vol. 52, No. 6, 1384–1386, 2010.
23. Li, R. L., B. Pan, T. Wu, and K. Lim, "A broadband printed dipole and a printed array for base station applications," *Proc. IEEE Int. Symp. AP-S*, 1–4, Jul. 2008.
24. Anguera, J., E. Martnez-Ortigosa, C. Puente, C. Borja, and J. Soler, "Broadband triple-frequency microstrip patch radiator combining a dual-band modified Sierpinski fractal and a monoband antenna" *IEEE Trans. Antennas Propag.*, Vol. 54, No. 11, 3367–3373, 2006.
25. Tefiku, F. and C. A. Grimes, "Design of broad-band and dual-band antennas comprised of series-fed printed-strip dipole pairs," *IEEE Trans. Antennas Propag.*, Vol. 48, No. 6, 895–900, 2000.
26. Li, R. L., T. Wu, B. Pan, K. Lim, J. Laskar, and M. M. Tentzeris, "Equivalentcircuit analysis of a broadband printed dipole with adjusted integrated balun and an array for base station applications," *IEEE Trans. Antennas Propag.*, Vol. 57, No. 7, 2180–2184, 2009.
27. Li, R. L., G. Dejean, J. Laskar, and M. M. Tentzeris, "Investigation of circularly polarized loop antennas with a parasitic element for bandwidth enhancement," *IEEE Trans. Antennas Propag.*, Vol. 53, No. 12, 3930–3939, 2005.
28. Jayasinghe, J. W., J. Anguera, D. N. Uduwawala, and A. Anújar, "A multipurpose genetically engineered microstrip patch antennas: Bandwidth, gain, and polarization," *Microw. Opt. Technol. Lett.*, Vol. 59, No. 4, 941–949, 2017.
29. Lin, S., Y. Tian, J. Lu, D. Wu, J. H. Liu, and H. J. Zhang, "A UWB printed dipole antenna and its radiation characteristic analysis," *Progress In Electromagnetics Research C*, Vol. 31, No. 31, 83–96, 2012.
30. Khan, S. and K. T. Wong, "Electrically long dipoles in a crossed pair for closed-form estimation of an incident sources polarization," *IEEE Trans. Antennas Propag. (Early Access)*, 1–14, 2019.